Numerical Modeling of Schottky Barrier Diode Characteristics

Daniel Splith,* Stefan Müller, Holger von Wenckstern, and Marius Grundmann

Herein, a comprehensive model is presented for the calculation of entire current–voltage (IV) characteristics of Schottky contacts (SCs). This treatment allows to analyze in detail the physical and technological origins of empirical fit parameters like the ideality factor. This model considers variations of the semiconductor net doping density in growth direction and barrier height inhomogeneities. The only input parameters required are the doping profile, the mean value, and the standard deviation of the barrier height distribution as well as material parameters. As measuring conditions like the integration time impact measured IV characteristics, similar sweep parameters as applied during a measurement are included in the model and proven to be necessary for the understanding of charging currents and the shift of the voltage for zero current. Using this model, various nonidealities reported in literature are explained. Further, the influence of differently doped interfacial layers on the characteristics is studied. Finally, the model is applied to multiple datasets of IV characteristics of SCs on different materials published in literature and from this laboratory, enabling a fundamental understanding of the origins of the nonidealities observed as well as the distinction between the contributions of different transport mechanisms to the total current.

1. Introduction

Since Walter Schottky explained the rectifying behavior of metal-semiconductor contacts by the formation of a charge carrier depletion layer in 1938,[1] different models have been developed to understand and evaluate the current–voltage (IV) characteristics of such Schottky contacts (SCs). At room temperature, thermionic emission (TE)[2] over the Schottky barrier is the dominating forward bias current transport mechanism for most materials. Only for low mobility materials diffusion currents[3] have to be

Dr. D. Splith, Dr. S. Müller, Dr. H. von Wenckstern, Prof. M. Grundmann
Felix Bloch Institute for Solid State Physics
Universität Leipzig
Linnéstr. 5, 04103 Leipzig, Germany
E-mail: daniel.splith@physik.uni-leipzig.de

The ORCID identification number(s) for the author(s) of this article can be found under https://doi.org/10.1002/pssa.202100121.

considered as well. However, the simple TE model does not suffice to describe entire experimental characteristics in most cases. Especially, the temperature dependence of the barrier height and ideality factors larger than 1.1 cannot be explained by TE. For this reason, several extensions had been made to the model: following the multicontact theory,[4–8] Werner and Güttler[9] introduced a model considering Gaussian distributed barrier height inhomogeneities to account for the temperature dependence of the effective barrier height and the ideality factor. Osvald[10] expanded this model by including individual series resistances for each path having a different barrier height, which can explain a nonexponential behavior in the forward direction. Furno et al.,[11] on the other hand, used the model of Werner and Güttler and the transfer matrix method developed by Ando and Itoh[12] to additionally account for the thermionic field emission (TFE) current as well as the image force lowering of laterally inhomogeneous SCs, which leads to a deformation of the barrier. Further, an inhomogeneous doping profile may impact band bending and is especially relevant for some wide bandgap semiconducting oxides like In_2O_3 or ZnO, as here the net doping density typically increases toward the surface.[13] On the other hand, by tuning the doping profile accordingly, the rectification of the SCs can be improved.[14] The models described earlier also assume a quasistatic measurement, thereby neglecting the charging current of the space charge region capacitance. Depending on the measurement conditions, this current may, however, be visible in the measured characteristics, especially for materials where SCs with high barrier heights and with that low saturation current are formed, e.g., on β-Ga_2O_3.

In this article, we present a numerical model for the calculation of the current through a laterally inhomogeneous SC by combining the extension of Osvald and Furno et al. as well as the possibility to calculate the currents for nonhomogeneous doping profiles leading to a spatial dependence of the band bending. In addition, the currents charging the space charge region capacitance are considered: even though most experimental IV characteristics published are nominally DC measurements, typically a voltage sweep is carried out, meaning that the voltage changes at a predefined rate depending on the measurement unit and settings. Potential rate-dependent dynamics are included in our model which allows to understand variations in characteristics induced by different sweep rates.

By fitting these calculated characteristics with the TE model commonly used for experimental characteristics, we investigated the influence of several input parameters of the model on the output parameters of the fit, allowing us to understand certain features and nonidealities observed for experimental characteristics reported in literature. Further, the model is applied to several characteristics of SCs published in literature as well as characteristics of our SCs fabricated on heteroepitaxial In_2O_3 and β-Ga_2O_3 thin films grown by pulsed laser deposition. Due to the good agreement between the simulated and the experimental characteristics, the physical and technological origins of nonidealities in the IV characteristics can be understood and the contributions of different transport mechanisms to the total current can be traced and distinguished.

2. Modeling of IV Characteristics

For the numerical calculation of the diode currents, the transfer matrix method[12] was used, similar to the approach of Furno et al.[11] However, the following extensions were implemented: inhomogeneous doping profile, lateral barrier height inhomogeneities[9] as well as lateral current spreading for paths of different barrier heights. For the latter, the model developed by Osvald,[10] where the series resistance is subdivided into a global series resistance R_{gl} and local series resistances R_{loc} for each current path of different barrier height (called R_C and R_P, respectively, in the original article), was implemented. In addition, the influence of measuring conditions, specifically the integration time during a full bias range sweep measurement was considered, which plays an important role for the charging current measurable for contacts with high barrier heights and low leakage current. Details on the individual parts of the model as well as their implementation can be found in the Supporting Information.[15]

To use this model, the parameters of the inhomogeneous barrier distribution, namely mean barrier height $\overline{\Phi}_{B,0}$ and the standard deviation σ_0 (at $V = 0\,V$) are necessary. These parameters can be determined from the temperature dependence of the effective barrier height Φ_B^{eff} determined by the fit of the IV characteristic with TE theory. This was used in two ways: First, we used predetermined values for the barrier parameters and used the fit with TE theory to show that the model is self-consistent. Then, we used the fit with TE theory to determine the barrier parameters of experimental datasets, used our model to calculate the diode characteristics and compared the calculated and the experimental characteristics to each other.

According to Rhoderick and Williams,[16] the current density in TE theory is given by

$$j = j_0 \exp\left(\frac{eV_A}{\eta k_B T}\right)\left[1 - \exp\left(-\frac{eV_A}{k_B T}\right)\right] \quad (1)$$

where

$$j_0 = A^* \frac{m_{eff}}{m_0} T^2 \exp\left(-\frac{\Phi_B^{eff}}{k_B T}\right) \quad (2)$$

Here, A^* is the Richardson constant and η is the ideality factor. For voltages larger than $3\frac{k_B T}{e}$, Equation (1) can be simplified to

$$j = j_0 \left[\exp\left(-\frac{eV_A}{\eta k_B T}\right) - 1\right] \quad (3)$$

V_A is the voltage applied at the SC. If we consider the series resistance R_s, V_A can be calculated from the overall voltage V by

$$V_A = V - jA_0 R_s \quad (4)$$

where A_0 is the area of the contact. By fitting IV characteristics with Equation (3), we can determine the effective barrier height Φ_B^{eff}, the ideality factor η, and the series resistance. Further, according to the theory of Werner and Güttler,[9] one can determine the mean barrier height $\overline{\Phi}_{B,0}$ and the standard deviation σ_0 (at $V = 0\,V$) of the Gaussian barrier distribution from a fit of the temperature dependence of the effective barrier height, using the following equation

$$\Phi_B^{eff} = \overline{\Phi}_{B,0} - \frac{\sigma_0^2}{2k_B T} \quad (5)$$

3. Investigation of Simulated Characteristics

As a first example, we used the model to simulate IV characteristics with predetermined values. With this, we demonstrate the information to be obtained from the model and investigate certain behaviors observed in literature as well as show the self-consistency of the model. If not stated otherwise, the predetermined values are: a homogeneous doping profile with $N_t = 1 \times 10^{16}\,cm^{-3}$ as well as $N_t = 1 \times 10^{18}\,cm^{-3}$, a mean barrier height of $\overline{\Phi}_{B,0} = 1.5\,eV$ and a standard deviation of $\sigma_0 = 0.15\,eV$. The characteristics were calculated in the range between $V = -3$ and $3\,V$ in steps of $0.015\,V$ for temperatures between $T = 50$ and $550\,K$. For the material parameters, the values for β-Ga_2O_3 ($m_{eff} = 0.28m_0$[17,18] and $\varepsilon_r = 10$[19]) were used.

3.1. Contributions to the Total Current

An example of such simulated IV characteristics is shown in **Figure 1** for $T = 300\,K$ for both doping concentrations. One advantage of the model is apparent immediately: the contributions of different transport mechanisms to the total current can be distinguished. While the forward direction is dominated by the TE current for both cases, in the reverse direction, the TFE current plays an important role for $N_t = 10^{18}\,cm^{-3}$ for voltages smaller than $-2\,V$. In addition, the charging current is increased compared with the charging current for $N_t = 10^{16}\,cm^{-3}$, as the capacitance of the SC is larger. Note that the combination of charging current, which increases with increasing voltage, and the TFE current, which increases with decreasing voltage, can lead to a local minimum of the absolute value of the current in the reverse voltage range. The total current is plotted for both positive and negative bias sweeping (PBS and NBS) meaning that the voltage is changed either from -3 to $3\,V$ or vice versa. While the currents due to the transport mechanisms stay the same, the sign of charging current j_C depends on the sweep direction. Figure 1 shows only the charging current for NBS. For PBS, it would be the same, but with a positive sign. This leads to a
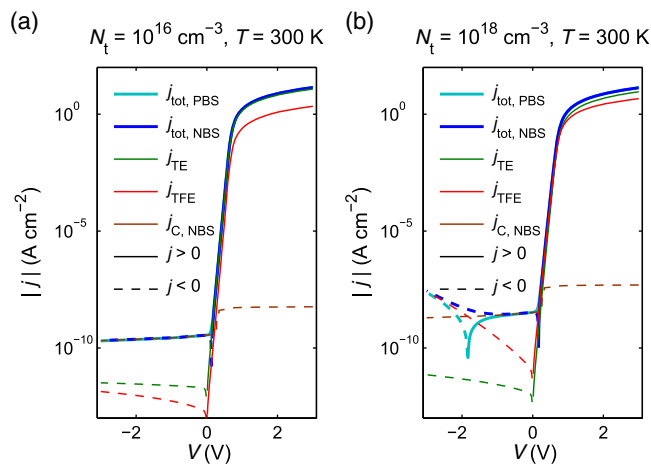
Figure 1. Simulated characteristics at $T = 300\,K$ for doping concentrations as labeled and $R_{gl} = 100\,\Omega$, $R_{loc} = 0\,\Omega$. In addition to the total current, the contributions of the individual currents considered here are plotted. The total current is shown for both PBS and NBS. The charging current is only shown for NBS. The lines are solid (dashed) for positive (negative) values of j.

Figure 2. Simulated characteristics at $T = 300\,K$ for a doping concentration of $N_t = 10^{18}\,cm^{-3}$, $R_{gl} = 100\,\Omega$, $R_{loc} = 0\,\Omega$, and different constant integration times Δt as indicated. The size of the voltage steps was 0.015 V. In addition to the total current, the contribution of the charging current is shown. The total current is shown for both PBS and NBS, the charging current only for NBS. For PBS, the sign of the charging current is opposite. The lines are solid (dashed) for positive (negative) values of j.

shift of the zero crossing of the total current in dependence on the sweep direction shown in Figure 1b: For NBS, the zero crossing is shifted to positive voltages, whereas for PBS, it is shifted to negative voltages to the point where the TFE current starts to dominate. A similar behavior is observed in experimental data for different materials.[20–25] The extent of the charging current depends primarily on the measurement conditions, more precisely on the sweep rate of the measurement, which depends on the voltage steps and the integration time of the measurement unit. Note that modern measurement units adjust the integration time dynamically in dependence on the current measured. This is also included in our model, leading to visible steps in the charging current in Figure 1. Details can be found in the Supporting Information.[15]

To demonstrate the influence of the charging current on the overall characteristic, IV characteristics were simulated with the same parameters, as in Figure 1b, but different, constant integration times are shown in **Figure 2**. The integration time was set to a constant value over the whole voltage range, as indicated in the graph. For $\Delta t = 1\,s$, the integration time in the reverse current range is the same as the maximum integration time for the characteristic in Figure 1b. Even if the integration time is increased by two orders of magnitude (leading to a two orders of magnitude longer measurement time in an experiment), the charging current is still visible in the characteristic. If one would start the measurement from $V = 0\,V$ and measure forward and reverse characteristic separately, the charging current would still be visible, however, no zero crossing would occur, as it is located left of $V = 0\,V$ for PBS and right of $V = 0\,V$ for NBS. In Figure 1a, no zero crossing is visible for the PBS, as the current stays positive over the whole voltage range. Note that this behavior is only observable when the sample is in equilibrium at the beginning of the measurement. Typically, the starting voltage is applied abruptly at the beginning of the measurement, meaning that the voltage changes from 0 V to the starting voltage in a short
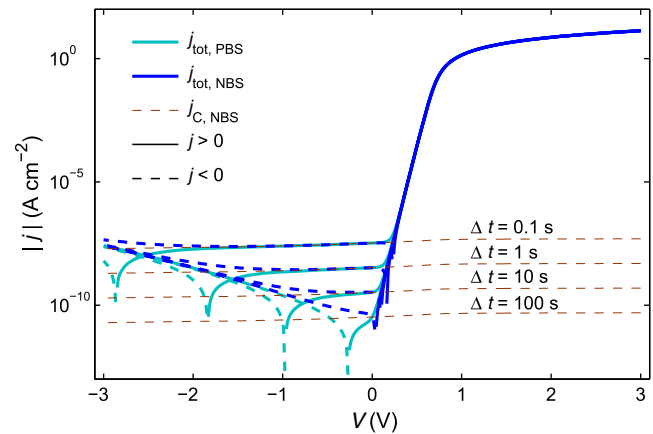
period of time, leading first to a negative charging current, which then changes sign in the subsequent measurement. Therefore, a zero crossing must appear, it should, however, be close to the starting voltage. In the following text, we concentrate on the simpler case of NBS, where this effect is negligible, as the current in forward direction is never dominated by the charging current.

3.2. Local Series Resistance

As the currents were calculated for each barrier height, we can easily apply the model developed by Osvald,[10] were the current through each path of different barrier heights is limited by a local series resistance R_{loc} and the current through all current paths is limited by the global series resistance R_{gl}. The equivalent circuit is shown in Figure S1, Supporting Information.[15] To demonstrate the influence of the local series resistance, in **Figure 3**, the IV characteristics are plotted for $N_t = 10^{18}\,cm^{-3}$ and $R_{gl} = 100\,\Omega$, but various values of R_{loc} for two different temperatures (a) $T = 100\,K$ and (b) $T = 300\,K$. As the influence of the series resistance is negligible for the reverse direction, only the forward direction is shown here. A large R_{loc} reduces the exponential slope of the IV characteristics and therefore increases the ideality factor η obtained by conventional curve fitting, as will be discussed later. From the plot one can clearly see that the influence of R_{loc} is stronger for smaller temperatures, as here a larger portion of the current is flowing over the lower barriers.

3.3. Barrier Height and Self-Consistency

The resulting curves were fitted with Equation (3) to determine the effective barrier heights. This was done for different temperatures and for $R_{loc} = 0\,\Omega$ and $0.1\,m\Omega$–$1\,k\Omega$, whereas R_{gl} was set constant to $100\,\Omega$. Note that the higher the resistance R_{loc} compared with R_{gl}, the more the calculated characteristic deviates from the standard model for TE using Equation (3). These curves
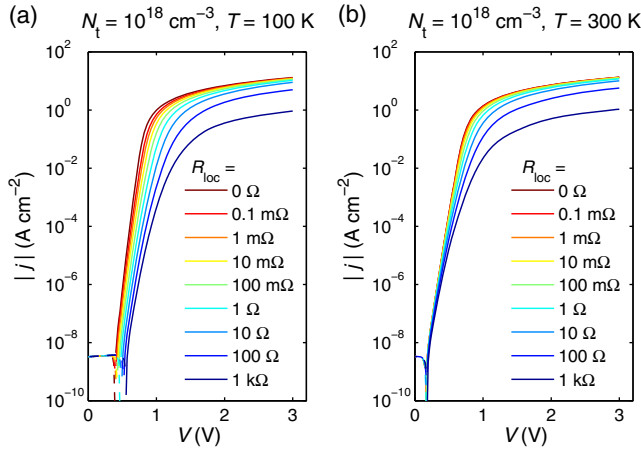
Figure 3. Simulated characteristics at a) $T = 100$ K and b) $T = 300$ K for $N_t = 10^{18}$ cm^{-3} and $R_{gl} = 100\,\Omega$. R_{loc} was varied between 0 and 0.1 mΩ–1 kΩ.

show a decrease in the slope with increasing voltages (or "rounding") in the region were the curve is expected to be linear in the semilog plot.[10] For these curves, the fit was only done in the exponential region, i.e., for voltages close to the zero crossing, as for this voltage range, the influence of R_{loc} is smallest (cf. Figure 3b). The determined effective barrier heights were then plotted versus T^{-1}. As an example, **Figure 4** shows the plot for $R_{loc} = 0.01\,\Omega$.

In addition to the curves with $\sigma_0 = 0.15$ eV, curves with $\sigma_0 = 0.10$ and $\sigma_0 = 0.20$ eV at $N_t = 10^{18}$cm^{-3} were calculated, fitted, and plotted in this figure for comparison. For $\sigma_0 = 0.15$ eV, the curves exhibit a linear behavior down to temperatures of $T = 170$ K ($1000/T \approx 5.9$ K^{-1}), as expected from theory according to Equation (5). For lower temperatures, a deviation from the linear dependence is observed. The same can be observed for $\sigma_0 = 0.10$ eV ($\sigma_0 = 0.20$ eV), however, here the deviation from the linear dependence occurs at lower (higher) temperatures compared with $\sigma_0 = 0.15$ eV.
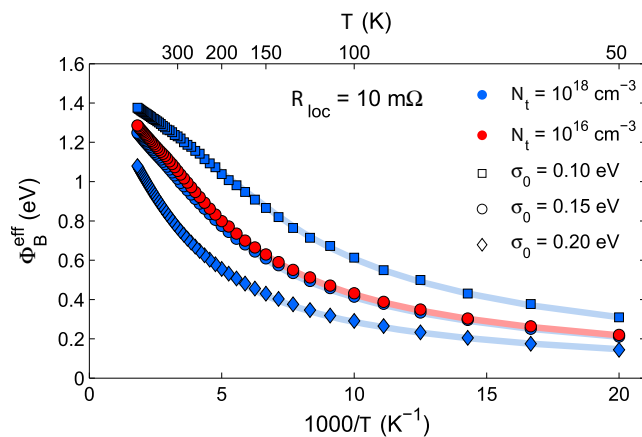

Figure 4. Effective barrier height in dependence on T^{-1} for $R_{loc} = 0.01\,\Omega$ determined from fits of the calculated characteristics for both doping concentrations and different values of σ_0 for $N_t = 10^{18}$ cm^{-3}. The light colored lines show the respective fits with Equation (6).

The deviation from the predicted linear dependence[9] is observed for several SCs on different materials, e.g., in previous studies[26–30] experimentally. To explain this behavior, usually a double Gaussian barrier distribution model proposed by Jiang et al.[31] is used. However, we find that the deviation from the linear dependence observed here is inherent to the modeled data, and it is unnecessary to invoke a double Gaussian barrier distribution. A strictly linear behavior could also lead to negative effective barrier heights for low temperatures, which would be unphysical.[32] Generally, as soon as a Gaussian barrier distribution is assumed, the question is how negative barrier heights need to be considered. Even though the distribution decreases strongly toward zero for high mean barrier heights and low standard deviations, the proportion of barrier heights below zero has not vanished. Physically, "barrier heights" below zero would mean that the local electron affinity of the semiconductor is larger than the work function of the metal for some patches of the contact. For those, however, an accumulation layer is expected to form instead of a space charge region, which would lead to an additional Ohmic current path. Such current paths can be considered by a parallel resistance, but should not be considered for TE and TFE currents. Therefore, we argue that the assumption of a full Gaussian distribution of barrier heights (with positive and negative values) is not correct. To avoid this problem, we propose two possible solutions: On the one hand, one could use another distribution function, that does not include negative values, e.g., the Gamma distribution. On the other hand, one could use the Gaussian distribution, but only for barrier heights larger than zero. For the simulations discussed here up to this point and in the following, the second approach was chosen. The good agreement between the temperature dependence of the effective barrier height observed for the simulated data and in literature confirms that this approach is valid. In fact, using the derivation of the temperature dependence of Werner and Güttler, but using 0 instead of $-\infty$ as the lower limit for the integration (in Equation (11) in the study by Werner and Güttler[9]), one obtains the equation

$$\Phi_B^{eff} = \overline{\Phi}_{B,0} - \frac{\sigma_0^2}{2k_B T} + k_B T \ln\left[1 + \mathrm{erf}\left(\frac{\overline{\Phi}_{B,0}}{\sqrt{2}\sigma_0}\right)\right]$$
$$- k_B T \ln\left[1 + \mathrm{erf}\left(\frac{\overline{\Phi}_{B,0} - \sigma_0^2/(k_B T)}{\sqrt{2}\sigma_0}\right)\right] \quad (6)$$

The first additional term stems from the condition that the integral over the distribution function equals 1, whereas the second one comes from the integration of the current weighted with the barrier distribution. For

$$T \gg T_b = \frac{\sigma_0^2}{k_B \overline{\Phi}_{B,0}} \quad (7)$$

the second term of the correction approaches the first, but with a negative sign, such that both terms cancel each other in this temperature range. Therefore, the equation given by Werner and Güttler is applicable here. This can also be shown using the Taylor expansion at $\frac{1}{T} = 0$. On the other hand, it can be shown that at low temperatures (from the Taylor expansion at $T = 0$), the correction terms approach $-\overline{\Phi}_{B,0} + \frac{\sigma_0^2}{2k_B T}$, i.e., Equation (5),

but with a minus sign, such that the effective barrier height approaches 0. Details can be found in the Supporting Information.[15] Note that, Equation (6) cannot explain all temperature dependencies of the effective barrier height observed in literature, especially not the one observed by Jiang et al., where the absolute value of the slope for the high temperature region is smaller than for the low temperature region.[31] In this cases, the assumption of a double Gaussian barrier distribution is needed to explain the observed behavior.

To demonstrate that the effective barrier height follows Equation (6), the data in Figure 4 are fitted with said equation. The results are shown in Figure 4 as light blue or red lines. From the fit, the values for the mean barrier height and the standard deviation of the barrier distribution were determined and compared with the predetermined input values. A good agreement between the initial values and the determined values can be observed for the three different values for sigma and both net doping densities investigated, as well as for various values of the local series resistance, showing that the model is self-consistent. Details can be found in the Supporting Information.[15] Similar to this approach, for $T^{-1} < T_b^{-1}$, the curves can be fitted linearly, leading to similar results for $\overline{\Phi}_{B,0}$ and σ_0.

As the capacitance is calculated in the model described earlier, we can easily extract capacitance–voltage curves from the calculated data. From those, the built-in voltage can be determined. By considering the difference between the Fermi energy and the conduction band minimum eV_n as well as the image force lowering, this value can be compared to the mean barrier height, which was used for the calculation. The values determined show an excellent agreement to the mean barrier height. More details can be found in the Supporting Information.[15]

3.4. Ideality Factor

Apart from the effective barrier height, the ideality factor, which is a measure for the voltage dependence of the barrier height, is a parameter discussed commonly in articles about SCs. Reasons for this voltage dependence can be manifold, but generally the image force lowering of the barrier is responsible for an increase in the ideality factor from 1 up to 1.1. Larger ideality factors can be accounted for by the inhomogeneous barrier distribution, especially when considering local series resistances.[10] As the ideality factor is not an input parameter for the model discussed here, we can use the model to investigate the influence of different parameters on the ideality factor determined by fitting the simulated characteristics. We conducted this investigation for the following input parameters into our model: the local series resistance, the standard deviation of the barrier distribution and the temperature.

In **Figure 5**, a plot of $\eta^{-1} - 1 = -\rho_1$ versus T^{-1} is shown for $N_t = 10^{18}$ cm^{-3}, $\sigma_0 = 0.15$ eV and different values of R_{loc}. According to Werner and Güttler,[9] a linear dependence is expected for such a plot. This linear dependence was in good approximation observed for all values of R_{loc} in the range between $T = 350$ and $T = 170$ K (corresponding to 2.9 and 5.9 K^{-1} in Figure 5). Note that the lower temperature boundary of the linear region is about the same as for the linear region of
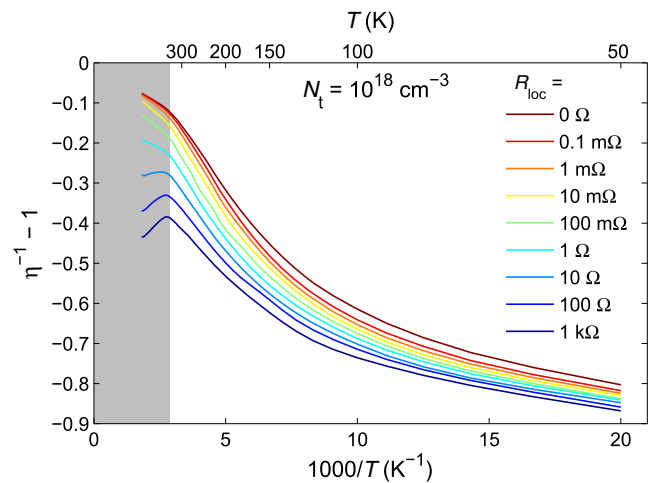

Figure 5. Plot of $\eta^{-1} - 1$ versus T^{-1} for $N_t = 10^{18}$ cm^{-3} and $\sigma_0 = 0.15$ eV for different values of R_{loc}. In the gray-shaded area, the range where the calculated characteristic shows an exponential behavior is small (which introduces large errors during fitting).

$\Phi_B^{eff}(T^{-1})$. We can fit this linear region to determine the voltage coefficients ρ_2 and ρ_3 of the mean barrier height and the standard deviation of the barrier distribution. The values range between -0.17 and 0.20 for ρ_2 and -0.017 and -0.011 eV for ρ_3 (for $R_{loc} = 0\,\Omega$ and $R_{loc} = 1\,k\Omega$, respectively). At lower temperatures, $\eta^{-1} - 1$ approaches -1, which should also be expected, as $\eta^{-1} - 1$ cannot be smaller than -1, when $\eta > 1$. This bent behavior is also observed in literature[27–29] and attributed again to a double Gaussian barrier distribution of the barrier height in most cases. Again, we note that this behavior is inherent to the data calculated for a diode with a single Gaussian barrier distribution and therefore, invoking a double Gaussian barrier distribution is not necessary and would even lead to false interpretation. For temperatures higher than 350 K (gray-shaded area) a kink is observed in the plot. To some extent, this kink has also to be expected: if ρ_2 is smaller than zero, a strict linear behavior would lead to values for $\eta^{-1} - 1$ larger than zero, which is not possible, as the ideality factor must be larger than 1. However, for high values of R_{loc} this kink is so pronounced that it is leading to a decrease in $\eta^{-1} - 1$ with increasing temperature. In general, the total current increases with increasing temperatures, leading to a stronger influence of the series resistances for lower voltages. In this case, this leads to smaller range in which the current increases exponentially, which is even smaller for higher values of R_{loc}. Therefore, the exact determination of the ideality factor is not possible here, which means that the kink, at least to some extent, is due to the fact that Equation (3) is not sufficient to accurately describe the simulated data. Note that for the calculation of the data, the resistances were kept constant. For an actual semiconductor, the resistances will decrease with increasing temperatures, counteracting this behavior to some extent.

On a real sample with multiple contacts, the value pairs of effective barrier height and ideality factor may be different for each contact. This can have various reasons. We would like to discuss the following two: the local series resistance R_{loc} or
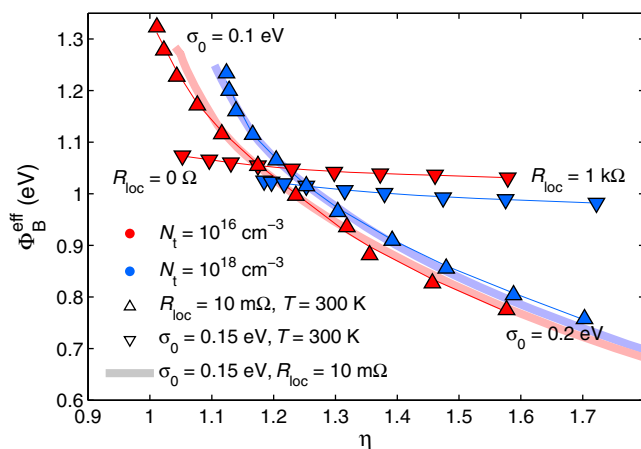
Figure 6. Effective barrier height in dependence on the ideality factor at 300 K for both doping concentrations. The change of the ideality factor is due to setting R_{loc} to $0\,\Omega$ and to values between $0.1\,m\Omega$ and $1\,k\Omega$ while keeping σ_0 constant at $0.15\,eV$ (∇) or changing σ_0 from 0.10 to $0.20\,eV$ while keeping R_{loc} constant at $10\,m\Omega$ (Δ). In addition, the data for $\sigma_0 = 0.15\,eV$ and $R_{loc} = 10\,m\Omega$ for varying temperatures are plotted for comparison (light blue and light red lines).

the standard deviation of the barrier distribution σ_0 may not be the same for all contacts due to sample inhomogeneities. In **Figure 6**, the effective barrier height is plotted in dependence on the ideality factor, both determined from the fit of the calculated data at a temperature of 300 K for both doping concentrations. The different values of η are either due to the different values of R_{loc}, which was set to $0\,\Omega$ (lowest ideality factor) and to values between $0.1\,m\Omega$ and $1\,k\Omega$ (highest ideality factor) while keeping σ_0 constant at $0.15\,eV$ (∇) or due to different values of σ_0, which was changed from $0.10\,eV$ (lowest ideality factor) to $0.20\,eV$ (highest ideality factor) while keeping R_{loc} constant at $10\,m\Omega$ (Δ). R_{gl} was set to $100\,\Omega$ for all points. For both doping concentrations, the same qualitative behavior is observed: While the changing of R_{loc} has mainly influence on the ideality factor, a change of σ_0 changes both the ideality factor and the effective barrier height.

For comparison, the effective barrier height in dependence on the ideality factor for $\sigma_0 = 0.15$ and $R_{loc} = 10\,m\Omega$ but determined at different temperatures is shown in Figure 6 (light blue or red lines). The dependency of the effective barrier height on the ideality factors for different values of sigma and for different temperatures seems to be qualitatively the same: for low ideality factors, the effective barrier height depends approximately linearly on the ideality factor. For higher values of η, the absolute value of the slope becomes smaller. This behavior is also often observed in literature: on the one hand for multiple contacts on the same sample[22,23,33,34] and on the other hand for temperature-dependent measurements on the same contact.[35,36] A similar behavior was also calculated by Schmitsdorf and Mönch[33] using patch-like inhomogeneities following Tung.[37] According to Schmitsdorf et al.,[38] the homogeneous barrier height can be determined by a linear extrapolation of the linear part to the value of the ideality factor achievable if the SC was homogeneous, with image force lowering as the only reason for a voltage dependence of the barrier. This value of

the ideality factor is typically between 1.01 and 1.1 (depending on the extend of the image force lowering). In literature, the homogeneous barrier height is often assumed to be the same as the mean barrier height. From our simulated data, however, we can conclude that this is not necessarily the case: only if R_{loc} is constant for the different contacts or for all temperatures, the extrapolation to determine the homogeneous barrier height in Figure 6 will result in values similar to the mean barrier height. Note also that the ideality factor from which on the absolute value of the slope becomes smaller depends on the doping concentration as well as the value of R_{loc} (not shown here). Therefore, the determination of the homogeneous barrier height provides a good lower boundary for the mean barrier height, but may differ from the actual mean barrier height. In turn, this further means that a large difference between the extrapolated value of the homogeneous barrier height and the mean barrier height or a small absolute value of the slope of $\Phi_B^{eff}(\eta)$ may hint toward inhomogeneous values of the local series resistance.

Other possible reasons for the scattering of the Φ_B^{eff} and η value pairs are, e.g., that the barrier distribution is not Gaussian shaped, the presence of doping inhomogeneities or that R_{loc} has not the same value for each current path. However, the influence of such nonidealities is beyond the scope of this article.

3.5. Influence of a Differently Doped Surface Layer

For wide bandgap semiconducting oxides the net doping density was reported to change within a thin subsurface region. For ZnO, for instance, this behavior depends on the orientation of the surface.[39] For Zn-polar ZnO, the surface has in tendency a lower electron concentration compared with the bulk, whereas the O-polar face typically shows increased carrier concentration. For In_2O_3, it was reported that the formation energy of the oxygen vacancy decreases drastically within the last monolayers toward the surface,[40] resulting in a surface electron accumulation layer. To judge on the impact of such changes of the net doping density on the IV characteristics, we modeled sample structures showing i) a decrease in the net doping density or ii) an increase in the net doping density within the first 10 nm from the interface by a factor of ten in comparison with the bulk value.

The results are shown in **Figure 7**. In Figure 7a, the characteristics were calculated for a structure where the first 10 nm are doped with $N_t = 10^{17}\,cm^{-3}$, whereas the bulk is doped with $N_t = 10^{18}\,cm^{-3}$. The resistances were set to $R_{gl} = 100\,\Omega$ and $R_{loc} = 10\,m\Omega$. While the influence on the forward characteristic is negligible, the TFE current is reduced in comparison with the characteristic with a constant doping profile. Consequently, the temperature dependence will be different to the case with homogeneous doping profile. In Figure 7b, the same is shown for the case where the first 10 nm are doped with $N_t = 10^{19}\,cm^{-3}$. Here, both, the forward and reverse characteristics are now dominated by the TFE current due to the smaller space charge region. For a reverse bias of $-2\,V$, the absolute current is increased by about four orders of magnitude in comparison with the curve calculated for a constant doping profile. Of course, the magnitude of the influence of the highly doped interfacial layer strongly
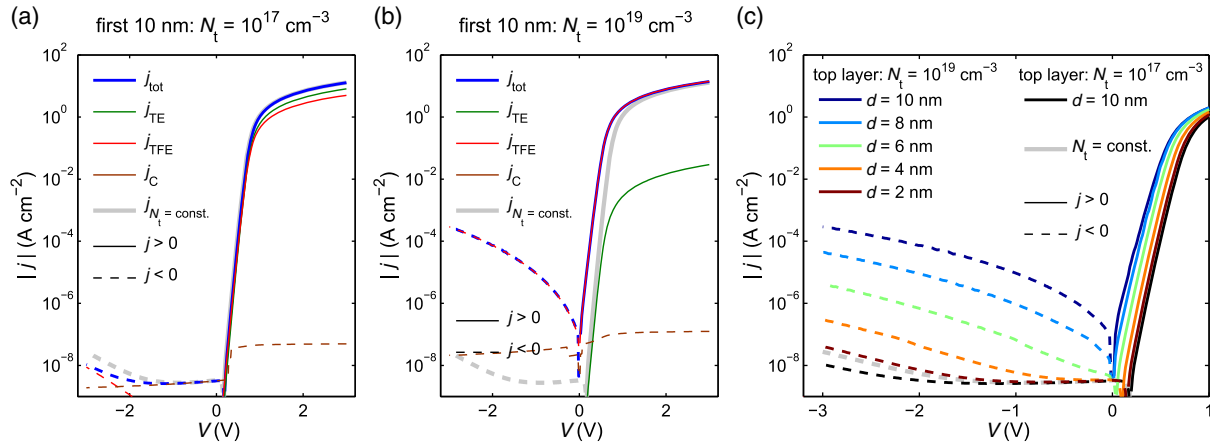
Figure 7. Influence of a differently doped interfacial layer on the IV characteristics at 300 K. The first 10 nm had a net doping density of a) 10^{17} cm^{-3} and b) 10^{19} cm^{-3}, whereas the bulk doping density is 10^{18} cm^{-3}. In addition to the total current, the calculated TE, TFE, and charging currents are plotted. For comparison, the calculated total current for a constant doping concentration of 10^{18} cm^{-3} is shown. (c) The total current is shown for different thicknesses d of the interfacial layer doped with a net doping density of 10^{19} cm^{-3}. In addition, the total current for the case were the 10 nm-thick interfacial layer is doped with 10^{17} cm^{-3} [cf. (a)] and for a constant doping concentration is shown for comparison. The lines are solid (dashed) for positive (negative) currents.

depends on the thickness of the later. This is shown in Figure 7c: Here the total current is shown for multiple thicknesses d of the interfacial layer, which had a net doping density of 10^{19} cm^{-3}, ranging between 2 and 10 nm. For comparison, also the total current for a constant net doping density and for a 10 nm-thick interfacial layer doped with $N_t = 10^{17}$ cm^{-3} are shown. When the highly doped interfacial layer is only 2 nm thick, the difference to the current for a constant doping concentration is very small. With increasing thickness however, the TFE current increases strongly, leading to a high reverse current as well as a slightly increasing forward current. The effective barrier height and the ideality factor, which were determined by fitting the calculated curves, change from 1.0 eV and 1.2 for $d = 2$ nm to 0.8 eV and 1.5 for $d = 10$ nm, respectively. Note that for the calculated currents shown here, the image force lowering was automatically compensated, so that the barrier height was 1.5 eV, independent of the net-doping density (see Supporting Information for details[15]). If this correction is not applied, the influence of the highly doped layer on the characteristics is even stronger, as the image force lowering is higher for high doping concentrations and large thicknesses, leading to lower barrier heights.

4. Comparison with Measured Data

To demonstrate how the model shown here can help to investigate and understand experimental results directly, it was applied to different datasets found in literature for different materials. In addition, it was used to investigate IV characteristics we measured on SCs on β-Ga$_2$O$_3$ and In$_2$O$_3$ thin films grown by pulsed laser deposition. Experimental details can be found in Section 6.

4.1. SCs on p-Type silicon

The data measured by Dökme et al.[41] on Al/p-Si Schottky barrier diodes was investigated by applying the model described earlier.

From the publication, the values of the barrier distribution ($\overline{\Phi}_{B,0} = 1.055$ and $\sigma_0 = 0.13$ eV) and the doping concentration ($N_t = 3.47 \times 10^{15}$ cm^{-3}) were taken. An effective mass of $0.27 m_0$ (effective Richardson constant of 32 A cm^{-2} K^{-2}) and a relative dielectric constant of 11.68 was assumed. The calculations were carried out for the same temperatures as the measurements in the article. Overall a good agreement between measured and simulated data was achieved over the whole temperature range.

In **Figure 8**, exemplary characteristics simulated with our model are shown for temperatures of 150, 250, and 375 K. For comparison, the data points measured by Dökme et al. were extracted from their publication and are also shown in
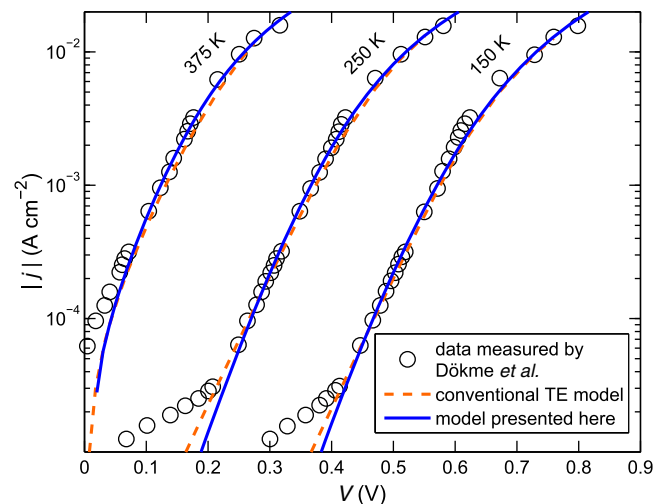

Figure 8. Characteristics of Al/p-Si Schottky barrier diodes measured by Dökme et al. in comparison with the characteristics simulated with the conventional TE model as well as the model described in this article. The parameters for calculating the characteristics were taken from the article of Dökme et al.

Figure 8. In addition, the curve of the conventional TE model (see Equation (3)) calculated from the effective barrier height and ideality factors determined by Dökme et al. is plotted. For current densities lower than $10^{-4}\,\mathrm{A\,cm^{-2}}$, a parallel current path (which could be considered by a parallel resistance in both models) dominates the total current. For currents higher than that, both models show good agreement with the measured data. Note, that as the ideality factor is not an input parameter in our model, the change in slope of the exponential region visible at different temperatures was accounted for by changing the ration between the local and global series resistance, which was fitted to the measured dataset for each temperature. This ratio decreases from 16% at $T = 150\,\mathrm{K}$ to 0.2% at $T = 375\,\mathrm{K}$. The model also allows to distinguish between the different contributions to the total current. In this case, TE dominates the current transport for all temperatures.

4.2. SCs on n-Type Gallium Arsenide

In their article from 1966, Padovani and Stratton presented a model for the field emission (FE) and TFE current in forward and reverse directions and used it to evaluate IV characteristics measured on gold-gallium arsenide SCs and gold-silicon SCs.[42] To demonstrate that our model is coherent with the model of Padovani et al., we simulated the IV characteristics of the gold-gallium arsenide SCs for temperatures between 20 and 160 °C and compare them with the measured data as well as the characteristics calculated with the model of Padovani et al.

First, to determine the barrier distribution, we fitted the forward characteristics measured by Padovani et al. for all temperatures from −200 to 160 °C with the model of Padovani et al. Here, the different temperature and voltage regions where the different currents (TE, TFE, and FE current) dominate the current were considered (See Supporting Information for details[15]). The only free parameters for this fit are the barrier height and the

ideality factor (for the TE current). A net-doping concentration of $N_t = 6.5 \times 10^{17}\,\mathrm{cm^{-3}}$ and an effective mass of $m_{eff} = 0.07 m_0$ were taken from the article of Padovani et al. A dielectric constant of 12.9 was assumed. According to the fit, for temperatures below −120 °C, the dominating transport mechanism is TE, which is due to the low effective barrier height due to the barrier height inhomogeneities. Therefore, the barrier distribution can be determined from the barrier heights in dependence on the temperature for temperatures below −120 °C. By fitting with Equation (6), a mean barrier height of 1.01 eV with a standard deviation of 0.097 eV was determined. These values as well as the parameters mentioned earlier were used to simulate the characteristics in the temperature range between 20 and 160 °C. In **Figure 9**a, the calculated characteristics for $T = 20$, 100, and 160 °C (as indicated by the labels and the brightness of the lines) are compared with the data measured by Padovani et al. as well as the characteristics calculated from the model of Padovani et al. For the latter, the barrier height from the fit of the forward direction was used for each temperature. Overall, a good agreement can be seen between the data measured by Padovani et al. and the characteristics calculated with the model described earlier. Small deviations can be observed in the forward direction, which may be due to the fact that the barrier distribution could only be calculated from the low temperature data. In the reverse direction, the overall trend of the measured data is also visible in the calculated characteristics. Deviations may be due to an inhomogeneous doping profile for voltages smaller than −1 V (CV data measured by Padovani et al. starts at −1 V). Comparing the characteristics calculated with the model of Padovani et al. to the data measured by Padovani et al. shows that in certain voltage ranges, the characteristics are modeled very well. However, especially when the FE current starts to dominate the characteristics (visible by the sudden increase in the current at $V = -2.2$, $V = -3.5$, and $V = -4.8\,\mathrm{V}$ for $T = 20$, $T = 100$, and $T = 160\,°\mathrm{C}$, respectively) deviations are evident. Comparing both models shows that the overall trend in reverse direction is modeled well. The
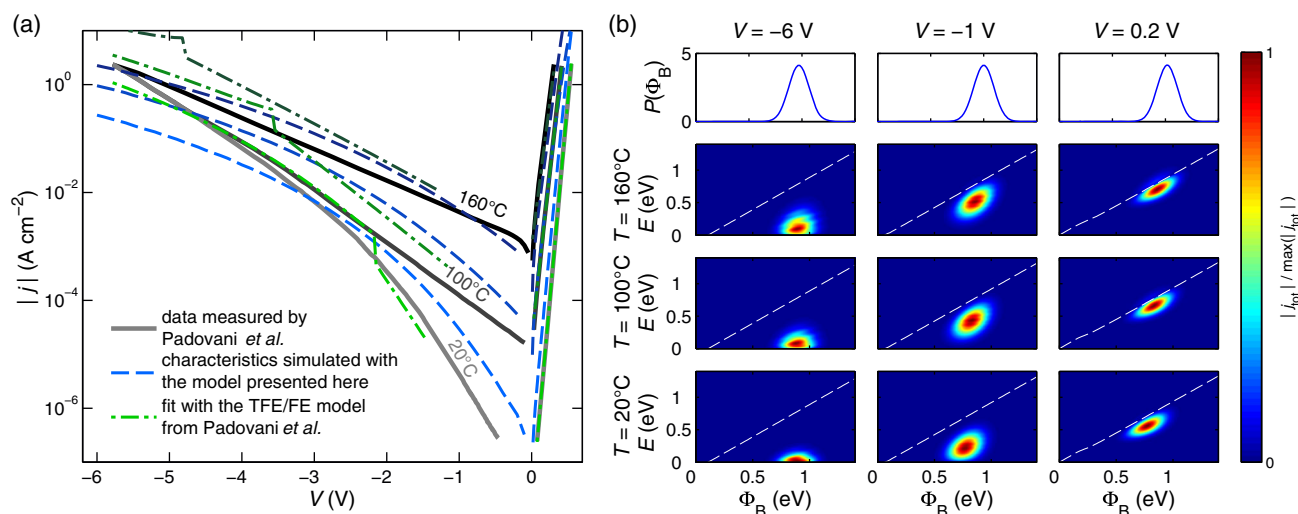

Figure 9. a) Characteristics of Au/n-GaAs Schottky barrier diodes measured by Padovani et al. in comparison to the characteristics simulated with the field emission/TFE model of Padovani et al. as well as the model described in this article. See text for details on the parameters. b) Normalized emission profiles in dependence on the energy relative to the Fermi energy of the metal and the barrier height of the barrier distribution for different voltages and temperatures. The first row shows the barrier distribution.

forward direction is modeled better by the model of Padovani. Note again that in the forward direction, the measured curve was fitted with the barrier height as free parameter, which changes from 0.95 eV at $T = 20\,°C$ to 0.89 eV at $T = 160\,°C$. For the characteristics calculated with the model described earlier, the barrier distribution determined from the low temperature data was used. A clear advantage of the model described in this article is, that it calculates the characteristic steady over the whole voltage range, whereas the equations of Padovani et al. give the characteristics for certain voltage regions, only.

Another advantage is that the model allows to investigate the different contributions to the total current. As an example, the normalized contribution to the current at $T = 20$, 100, and $160\,°C$ and $V = -6$, -1, and -0.2 V is shown in Figure 9b in dependence on the barrier height Φ_B and the energetic position E (referred to as emission profiles in the following). Here, $E = 0$ eV corresponds to the Fermi energy of the metal. The data are weighted with the barrier distribution function, which is shown in the first row (image force lowering is considered). The white line in the individual subfigures shows the energetic position of the barrier height after image force lowering. For all subfigures shown here, the maximum of the distribution lies below the white line, indicating that the dominating transport mechanism is either TFE or field emission. With increasing temperature, the maximum of the distribution shifts toward higher energies and slightly toward higher barrier heights. With decreasing voltage, the maximum shifts toward lower energies, leading to field emission at $V = -6$ V (i.e., emission close to $E = 0$ eV, the Fermi energy of the metal).

4.3. SCs on n-Type Gallium Nitride

Another dataset investigated with the model described earlier is the data measured by Jeong et al.[43] on Ag/Ni/n-GaN Schottky barrier diodes for temperatures ranging from 200 to 400 K. In the article, the authors attribute the reverse current to the Poole–Frenckel effect.

We applied the model described earlier to the data. For this a mean barrier height of 1.23 eV and a standard deviation of 0.15 eV as determined by Jeong et al. was used. According to Equation (7), we can expect a linear dependence of the effective barrier height for temperatures larger than ≈ 210 K, so the determination of the mean barrier height and the standard deviation of the barrier distribution by a linear fit is justified here. The following parameters were also taken from the article: a net doping density of 10^{18} cm^{-3}, an effective mass of 0.2 m_0. A dielectric constant of 8.9 was assumed. The results of the simulations are shown in **Figure 10**a in comparison with the measured data for the temperatures 200, 300, and 400 K as indicated by the labels and the brightness of the lines. Overall, the trend of the measured data is well reflected in the simulated data, with a good agreement in the forward direction and reverse currents at least in the same order of magnitude. A closer look into the simulated data shows that TFE is the dominating transport mechanism. For comparison, the forward direction of the characteristics were also fitted with the model of Padovani et al. Again, the only free parameter is the barrier height for each temperature. A significant increase in the barrier height can be observed from 0.81 eV at $T = 200$ K to 1.02 eV at $T = 400$ K. The temperature dependence of the barrier height indicates that barrier height inhomogeneities may play an important role. The characteristics calculated for the whole voltage range with the model of Padovani et al. are shown as green lines in Figure 10a. The respective barrier heights for the calculations were taken from the fit of the forward direction. This leads to a poor agreement between the measured data and the calculated data in the reverse direction. In addition to the fact that between 0 and about -1 V, the model of Padovani predicts the TE current to be dominant, which would lead to currents significantly smaller than the currents measured, especially for $T = 200$ K it can be seen that the
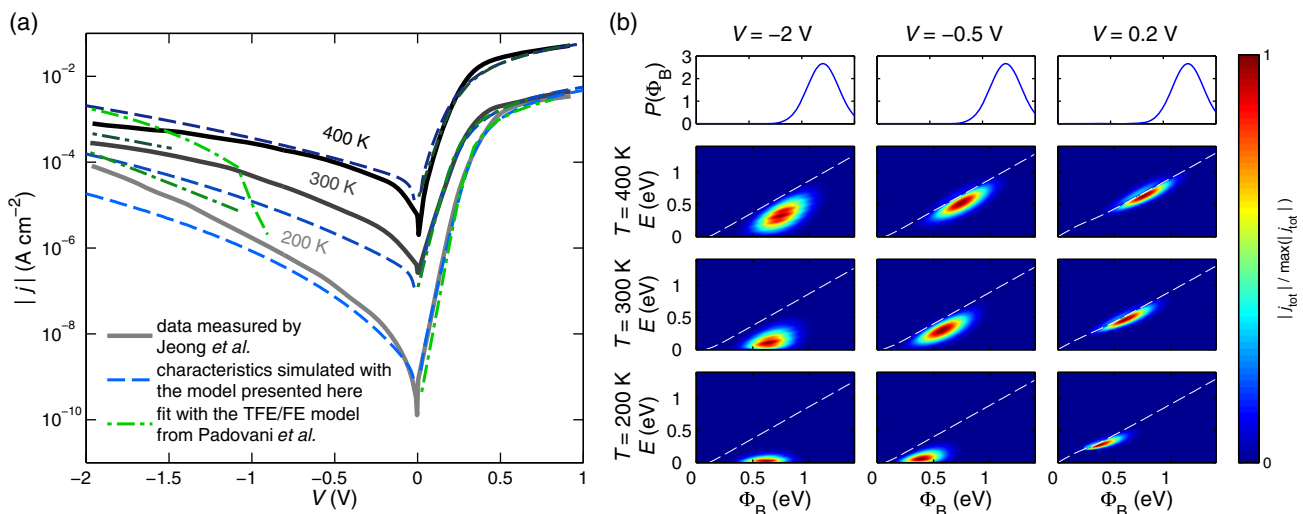

Figure 10. a) Characteristics of Ag/Ni/n-GaN Schottky barrier diodes measured by Jeong et al. in comparison with the characteristics simulated with the field emission/TFE model of Padovani et al. as well as the model described in this article. See text for details on the parameters. b) Normalized emission profiles in dependence on the energy relative to the Fermi energy of the metal and the barrier height of the barrier distribution for different voltages and temperatures. The first row shows the barrier distribution.

reverse current is far too high. This is due to the small barrier height determined at this temperature. Why the model of Padovani fails here can be easily seen from the data calculated with our model: the emission profiles in dependence on the energy relative to the Fermi level of the metal and the barrier height of the barrier distribution are shown in Figure 10b for different temperatures and voltages. A clear shift of the barrier height position of the current maximum with increasing temperature is visible for voltages of -0.5 and $0.2\,V$. For $-2\,V$, this shift is significantly smaller. This means that due to the inhomogeneity of the barrier height, different effective barrier heights dominate the current for different voltages. Therefore, the barrier distribution cannot be neglected here. In addition, a clear shift of the current maximum toward higher energy with increasing temperature is visible, but the maximum stays below the barrier height (after image force lowering, white line), meaning that TFE is dominant even for high temperatures. For low temperatures, the maximum is close to $E = 0\,eV$ (or $E = 0.2\,eV$ at $V = 0.2\,V$), meaning that field emission is dominant here.

Therefore, due to the comparably large standard deviation of the barrier distribution, it is not possible to model the data presented by Jeong et al. with the equations of Padovani et al., but with the model described earlier. As mentioned previously, Jeong et al. attributed the reverse current to Poole–Frenkel emission, which would typically be expected only for large electric fields. Upon closer inspection, their argument that the slope of the reverse current is close to the slope expected for Poole–Frenkel emission, does not hold, because the slope of the experimental data is a about a factor of 2 higher than the expected theoretical value (cf. Figure 8 in the study by Jeong et al.[43]). The good agreement between the curves simulated here and the data measured by Jeong et al. suggests that the dominating transport mechanism in reverse direction is TFE over a laterally inhomogeneous barrier.

4.4. Pt-SCs on In₂O₃ Thin Films

The model was used to calculate characteristics of Pt/In₂O₃ Schottky diodes having a nonhomogeneous doping profile. In₂O₃ is a material best known in its highly Sn-doped, highly conducting form used as a transparent electrode. In recent years, the interest in the semiconducting properties of In₂O₃ arose due to its high electron mobility. However, the realization of devices is not straightforward due to a surface electron accumulation layer (SEAL). Only recently, first SCs were realized using a reactive sputtering process,[44] as an oxygen plasma treatment is capable of removing the SEAL.[45] Here, we investigated nominally undoped thin films with a Mg-doped top layer of thickness d or without such a layer ($d = 0$). As Mg acts as an acceptor in In₂O₃, the net-doping density is reduced toward the surface by the Mg-doped layer. Experimental details can be found in the Section 6.

In **Figure 11**, characteristics of reactively sputtered Pt SCs on the three different sample structures are shown. The thickness of the Mg-doped layer strongly influences the characteristics of the SCs: For the sample without the Mg-doped layer, the current in reverse direction is less than two orders of magnitude smaller than the current in forward direction, whereas for a thickness
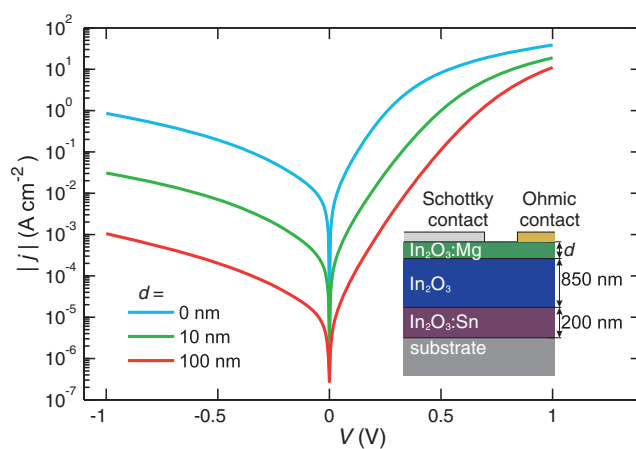
Figure 11. Measured characteristics of Pt-SCs on In₂O₃ thin films for different thicknesses of the Mg-doped layer. The inset shows a cross-section of the sample structure. The tin-doped layer is used as a back contact layer to reduce the series resistance.

of $100\,nm$, rectification ratios of 4 orders of magnitude are achieved.

The fit of the forward direction of the characteristic for $d = 0\,nm$ using Equation (3) yields an effective barrier height of about $0.5\,eV$. For $d = 10\,nm$, the current in reverse direction as well as the current in forward direction up to a voltage of $0.5\,V$ is reduced by almost two orders of magnitude. For $V > 0.5$, the curve approaches the characteristic for $d = 0\,nm$, but the current is still lower, hinting to a higher series resistance. The effective barrier height would be about $0.6\,eV$ here. With $d = 100\,nm$, the current for $V < 0.5\,V$ decreases another order of magnitude, whereas the current close to $V = 1\,V$ decreases only slightly. The effective barrier height is almost $0.7\,eV$. The increase in the effective barrier height determined with Equation (3) cannot be explained with the image force lowering due to the higher net doping density alone, especially since the net doping density of the top layer is the same for $d = 10$ and $d = 100\,nm$.

To understand this behavior qualitatively, we used the model described earlier. An effective mass of $m_{eff} = 0.3\,m_0$[46,47] and a relative dielectric constant of $\varepsilon_r = 8.9$[48] were used. As the evaluation of the parameters for the simulation from the measured data is not straightforward, the following assumptions have been made: We assumed that the barrier distribution (without image force lowering) is the same for all three values of d and that the doping profile is step-like. The barrier distribution was determined from a temperature-dependent IV measurement on the sample with $d = 100\,nm$ and evaluation by Equation (3) and (5) in the linear region to be $\overline{\Phi}_{B,0} = 1.28$ and $\sigma_0 = 0.18\,eV$. As the effect of image force lowering may be different for different values of d, we calculated the mean barrier height without image force lowering ($1.43\,eV$) and disabled the automatic compensation of image force lowering in the program (see Supporting Information for details[15]). By carrying out capacitance–voltage measurements on SCs fabricated on Mg-doped thin films, the net doping density for such thin films was determined to be $3 \times 10^{18}\,cm^{-3}$. Similar

measurements are not conclusive for nominally undoped thin films due to the high leakage current. Hall-effect measurements are also not conclusive due to the SEAL. Therefore, we simulated IV curves for $d = 0$ nm for different net doping densities.

A net doping density of 1×10^{19} cm^{-3} yields the best agreement to the measured data. Using these values, IV characteristics at room temperature for $d = 10$ and $d = 100$ nm were calculated.

In **Figure 12**, the calculated currents for a Pt-SC on an In$_2$O$_3$ thin film using the values mentioned earlier are plotted for the three different doping profiles, namely for a) a sample without a Mg-doped layer, b) a sample with a Mg-doped layer with a thickness of 10 nm, and c) for a sample with a 100 nm-thick Mg-doped layer. In addition to the total current j_{tot}, the contributions of the different transport mechanisms are shown. For all doping profiles, the TFE current is the dominant current. The TE current is at least about two orders of magnitude smaller than the TFE current and therefore negligible. From the simulation, also the space charge region width can be determined, which increases systematically from 11 nm for $d = 0$ to 14 nm for $d = 10$ and to 20 nm for $d = 100$ nm, as expected.

In addition to the calculated currents, measured data from Pt-SCs on the respective sample structures are shown. R_{loc} and R_{gl} of the calculated curves were fitted to best match the measured data in forward direction. While the value of R_{gl} is about constant at 25 Ω for all three diodes, the value of R_{loc} seems to strongly depend on the sample structure: For a sample without a Mg-doped layer, R_{loc} is very small and negligible compared with R_{gl}. For $d = 10$ nm, R_{loc} is increased, but still below 1% of R_{gl}. The value of the fitted R_{loc} for $d = 100$ nm however is about 20% of R_{gl}. This behavior is as expected: due to the higher resistance of the Mg-doped layer, the resistance of the respective current paths through the space charge region increases with increasing thickness of the Mg-doped layer, whereas the other resistances (e.g., resistance of the back contact layer, contact

resistances, and so on) stay about the same. Overall, the calculated curves show a good agreement with the measured characteristics. The biggest difference between the two is observed for $d = 10$ nm, especially in the reverse direction. This can however be explained by the strong influence of the exact thickness of the Mg-doped layer: since the thickness is only estimated from the growth rate, the value might actually be smaller. In addition, atomic-force microscopy shows that the root-mean-square layer roughness is about 2 nm. Due to the exponential dependence of the TFE current on the width of the space-charge region, current paths with a lower thickness of the Mg-doped layer would be preferred. Therefore, similar to the effective barrier height, the effective thickness of the Mg-doped layer may be smaller than 10 nm, leading to a higher current in the reverse direction.

While some assumptions were made to simulate the data, the good agreement between measured and calculated curves shows that the behavior can be explained by i) the influence of different R_{loc} for different doping profiles on the forward current and ii) the influence of the doping profile on the space charge region width and with that the current due to TFE.

Further, the same model was used in the study by Michel et al.[13] to understand differences between barrier heights determined by X-ray photoelectron spectroscopy (XPS) measurements and barrier heights determined from IV measurements for inertly or reactively sputtered Pt contacts on oxygen plasma-treated or untreated In$_2$O$_3$ thin films grown by plasma-assisted molecular beam epitaxy on c-plane sapphire. While the XPS measurements indicated that for the inertly sputtered contacts on the oxygen plasma-treated thin film, a barrier with a height of about 0.5 eV forms, no rectification was observed in the IV characteristics. Further, for the reactively sputtered contacts on the untreated thin film, a barrier height of about 0.9 eV was determined by XPS, whereas the homogeneous barrier height, determined from the IV characteristics was about 0.6 eV. We used our model to calculate characteristics and used
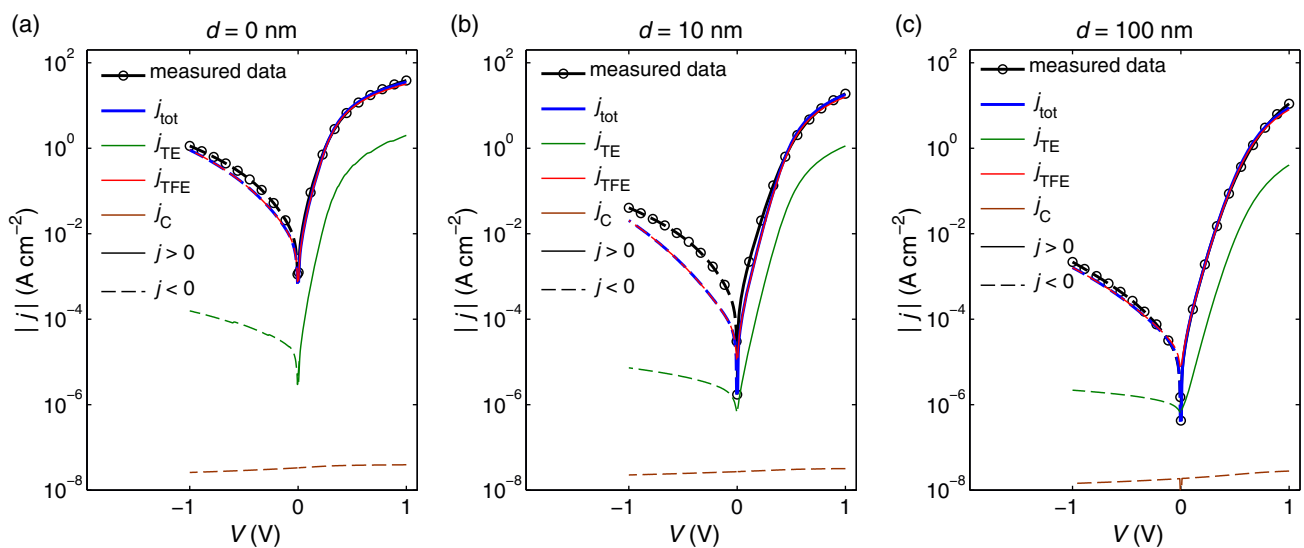

Figure 12. Characteristics calculated from the mean barrier height and standard deviation determined by the temperature-dependent IV measurements on a sample with a 100 nm-thick Mg-doped layer for a) $d = 0$ nm, b) $d = 10$ nm, and c) $d = 100$ nm. In addition to the total current, the calculated TE, TFE, and charging currents are plotted. The lines are solid (dashed) for positive (negative) currents.

the barrier heights determined by XPS as mean barrier heights. From the calculation, we find for the first case, that for a barrier of 0.5 eV, the current due to TFE is so high that also for the calculated data, no rectification can be observed. While in our calculated characteristic for a mean barrier height of 0.9 eV, TE current is also the dominating transport mechanism, the current in reverse direction is reduced significantly in comparison with the former case, resulting in a rectifying characteristic. For both cases, the calculated characteristics are similar to the experimental characteristics, which resolved the apparent disagreement between the XPS and current transport measurements. This again demonstrates how the model presented here can be used to understand the physical origin of measured IV characteristics in more detail.

4.5. Cu-SCs on β-Ga₂O₃ Thin Films

The application of the described model for the evaluation of experimental data of Cu-Schottky diodes on β-Ga₂O₃ thin films was published in previous studies.[49] Exemplary calculated characteristics in comparison with the measured characteristics for two temperatures (30 and 150 °C) as well as some details can be found in the Supporting Information.[15] The model shows a good agreement with measured data for all temperatures investigated. From a fit, the local and global series resistances were determined in dependence on the temperature. While the global series resistance can be attributed to a defect with an activation energy of 180 meV, the local series resistance shows a step-like behavior, possibly due to potential barriers at grain boundaries.

5. Conclusion

In conclusion, we combined various models describing different current transport mechanisms and their nonidealities into a single unified model to calculate the entire IV characteristics of Schottky barrier diodes. The model considers TE and TFE currents using the spatial dependence of the band diagram. The band diagram cannot only be calculated for homogeneous doping, but for doping profiles as well. In addition, the charging of the space charge region capacitance is accounted for. Also, barrier height inhomogeneities as well as current spreading are included into this model.

On the basis of this numerical model commonly observed nonidealities such as i) bending of forward characteristics in semilog representation, ii) different $\Phi_B^{eff}(\eta)$ dependencies including bent curves, linear dependence, and even an almost η-independent behavior, iii) bending of $\Phi_B^{eff}(T^{-1})$ plots for low temperatures, iv) dependence of the voltage for zero current on sweep direction, v) dependence of the voltage for zero current on the sweep parameters, and vi) different signs of the reverse current slope are qualitatively and quantitatively understood.

Further, the influence of a differently doped interfacial layer was investigated using the numerical model. Especially for a layer with a higher doping concentration, the calculated characteristics change significantly: the layer leads to an increase in TFE current and therefore an increased reverse and forward currents.

Finally, our model was used to investigate characteristics published in literature and characteristics of devices measured by us. In both cases, the model shows a good agreement to the measured data and allows to gain a deeper physical understanding of the measured characteristics. Especially the fact that the model allows to distinguish between the different contributions to the total current allows to identify the parameters limiting the rectification and therefore enables further optimization of the diodes.

6. Experimental Section

Cu-SCs on β-Ga₂O₃ Thin Films: The β-Ga₂O₃ thin films were grown by PLD on a highly Ga-doped ZnO layer, which acts as a back contact layer for the SCs.[20] The ZnO layer was grown on top of an a-plane sapphire substrate. SCs were fabricated using photolithography and DC-sputtering of Cu and subsequently characterized in a Süss waferprober system P200 using an Agilent 4155C precision semiconductor parameter analyzer for temperatures between 30 and 150 °C.

Pt-SCs on In₂O₃ Thin Films: The In₂O₃ thin films used for this study were grown by PLD on c-plane sapphire substrates. Similar to von Wenckstern et al.,[50] different thicknesses of Mg-doped layer grown from a target with 1 wt% MgO were deposited on top of the nominally undoped thin film. As Mg acts as an acceptor in In₂O₃, the Mg was expected to reduce the net doping density and therefore increase the space charge region width. In this study, we investigated three different layouts, namely with thicknesses of about $d = 10$, $d = 100$ nm of the Mg-doped layer and without a Mg-doped layer on top ($d = 0$ nm). The thicknesses were estimated from the growth rate of Mg-doped thin films. To reduce the series resistance, a tin-doped In₂O₃ layer grown from a target with 1 wt% SnO₂ was deposited underneath the nominally undoped layer to realize a vertical diode, similar to Schmidt et al.[14] Subsequently, circular Pt-SCs were fabricated using photolithography and a reactive sputtering process, similar to von Wenckstern et al.[44] IV characteristics were measured in a Süss waferprober system P200 using an Agilent 4155C precision semiconductor parameter analyzer, capacitance–voltage measurements were carried out with an Agilent 4294A precision impedance analyzer.

Supporting Information

Supporting Information is available from the Wiley Online Library or from the author.

Conflict of Interest

The authors declare no conflict of interest.

Data Availability Statement

Data available on request from the authors.

[1] W. Schottky, *Naturwissenschaften* **1938**, *26*, 843.

[2] H. A. Bethe, *Theory of the Boundary Layer of Crystal Rectifiers*, Report 43-12. Radiation Laboratory, Massachusetts Institute of Technology **1942**.

[3] W. Schottky, E. Spenke, *Wissenschaftliche Veröffentlichungen aus den Siemens-Werken*, Vol. *18*, chapter Zur quantitativen Durchführung der Raumladungs- und Randschichttheorie der Kristallgleichrichter, Springer Berlin Heidelberg, Berlin, Heidelberg **1939**, pp. 225–291.

[4] H. J. Yearian, *Phys. Rev.* **1946**, *69*, 682.

[5] R. G. Sachs, *Phys. Rev.* **1946**, *69*, 682.

[6] V. A. Johnson, R. N. Smith, H. J. Yearian, *Phys. Rev.* **1946**, *69*, 682.

[7] V. A. Johnson, R. N. Smith, H. J. Yearian, *J. Appl. Phys.* **1950**, *21*, 283.

[8] H. J. Yearian, *J. Appl. Phys.* **1950**, *21*, 214.

[9] J. H. Werner, H. H. Güttler, *J. Appl. Phys.* **1991**, *69*, 1522.

[10] J. Osvald, *J. Appl. Phys.* **2006**, *99*, 033708.

[11] M. Furno, F. Bonani, G. Ghione, *Solid-State Electron.* **2007**, *51*, 466.

[12] Y. Ando, T. Itoh, *J. Appl. Phys.* **1987**, *61*, 1497.

[13] J. Michel, D. Splith, J. Rombach, A. Papadogianni, T. Berthold, S. Krischok, M. Grundmann, O. Bierwagen, H. von Wenckstern, M. Himmerlich, *ACS Appl. Mater. Interfaces* **2019**, *11*, 27073.

[14] F. Schmidt, D. Splith, S. Müller, H. von Wenckstern, M. Grundmann, *Phys. Status Solidi B* **2015**, *252*, 2304.

[15] Supplemental Material: Unified Numerical Model for Schottky Barrier Diode Characteristics.

[16] E. H. Rhoderick, R. H. Williams, *Monographs in Electrical and Electronic Engineering*, Clarendon Press, Oxford, UK **1988**.

[17] M. Mohamed, C. Janowitz, I. Unger, R. Manzke, Z. Galazka, R. Uecker, R. Fornari, J. R. Weber, J. B. Varley, C. G. Van de Walle, *Appl. Phys. Lett.* **2010**, *97*, 211903.

[18] J. B. Varley, J. R. Weber, A. Janotti, C. G. Van de Walle, *Appl. Phys. Lett.* **2010**, *97*, 142106.

[19] M. Passlack, N. E. J. Hunt, E. F. Schubert, G. J. Zydzik, M. Hong, J. P. Mannaerts, R. L. Opila, R. J. Fischer, *Appl. Phys. Lett.* **1994**, *64*, 2715.

[20] D. Splith, S. Müller, F. Schmidt, H. von Wenckstern, J. J. van Rensburg, W. E. Meyer, M. Grundmann, *Phys. Status Solidi A* **2014**, *211*, 40.

[21] M. W. Allen, X. Weng, J. M. Redwing, K. Sarpatwari, S. E. Mohney, H. von Wenckstern, M. Grundmann, S. M. Durbin, *IEEE Trans. Electron Devices* **2009**, *56*, 2160.

[22] S. Müller, H. von Wenckstern, F. Schmidt, D. Splith, R. Heinhold, M. Allen, M. Grundmann, *J. Appl. Phys.* **2014**, *116*, 194506.

[23] S. Müller, H. von Wenckstern, F. Schmidt, D. Splith, F.-L. Schein, H. Frenzel, M. Grundmann, *Appl. Phys. Express* **2015**, *8*, 121102.

[24] H. von Wenckstern, D. Splith, A. Werner, S. Müller, M. Lorenz, M. Grundmann, *ACS Comb. Sci.* **2015**, *17*, 710.

[25] M. Garg, T. R. Naik, C. S. Pathak, S. Nagarajan, V. R. Rao, R. Singh, *Appl. Phys. Lett.* **2018**, *112*, 163502.

[26] Y.-L. Jiang, G.-P. Ru, F. Lu, X.-P. Qu, B.-Z. Li, S. Yang, *J. Appl. Phys.* **2003**, *93*, 866.

[27] B. Abay, *J. Alloys Compd.* **2010**, *506*, 51.

[28] N. Tuğluoğlu, Ö. F. Yüksel, H. Şafak, S. Karadeniz, *Phys. Status Solidi A* **2012**, *209*, 2313.

[29] V. R. Reddy, V. Janardhanam, C.-H. Leem, C.-J. Choi, *Superlattices Microstructures* **2014**, *67*, 242.

[30] H. Kim, S. H. Kim, C. Y. Jung, Y. Cho, D.-W. Kim, *Vacuum* **2015**, *121*, 125.

[31] Y.-L. Jiang, G.-P. Ru, F. Lu, X.-P. Qu, B.-Z. Li, W. Li, A.-Z. Li, *Chin. Phys. Lett.* **2002**, *19*, 553.

[32] J. Osvald, *Semicond. Sci. Technol.* **2003**, *18*, L24.

[33] R. F. Schmitsdorf, W. Mönch, *Eur. Phys. J. B* **1999**, *7*, 457.

[34] S. Müller, H. von Wenckstern, O. Breitenstein, J. Lenzner, M. Grundmann, *IEEE Trans. Electron Devices* **2012**, *59*, 536.

[35] W. Mönch, *J. Vac. Sci. Technol. B* **1999**, *17*, 1867.

[36] M. K. Hudait, S. B. Krupanidhi, *Phys. B* **2001**, *307*, 125.

[37] R. T. Tung, *Phys. Rev. B* **1992**, *45*, 13509.

[38] R. F. Schmitsdorf, T. U. Kampen, W. Mönch, *J. Vac. Sci. Technol. B* **1997**, *15*, 1221.

[39] M. W. Allen, P. Miller, R. J. Reeves, S. M. Durbin, *Appl. Phys. Lett.* **2007**, *90*, 062104.

[40] A. Walsh, *Appl. Phys. Lett.* **2011**, *98*, 261910.

[41] I. Dökme, Ş. Altindal, M. M. Bülbül, *Appl. Surf. Sci.* **2006**, *252*, 7749.

[42] F. A. Padovani, R. Stratton, *Solid-State Electron.* **1966**, *9*, 695.

[43] J.-Y. Jeong, V. Janardhanam, H.-J. Yun, J.-H. Lee, J.-Y. Kim, K.-H. Shim, C.-J. Choi, *Jpn. J. Appl. Phys.* **2014**, *53*, 8S308.

[44] H. von Wenckstern, D. Splith, F. Schmidt, M. Grundmann, O. Bierwagen, J. S. Speck, *APL Mater.* **2014**, *2*, 046104.

[45] O. Bierwagen, J. S. Speck, T. Nagata, T. Chikyow, Y. Yamashita, H. Yoshikawa, K. Kobayashi, *Appl. Phys. Lett.* **2011**, *98*, 172101.

[46] N. Preissler, O. Bierwagen, A. T. Ramu, J. S. Speck, *Phys. Rev. B* **2013**, *88*, 085305.

[47] H. Fujiwara, M. Kondo, *Phys. Rev. B* **2005**, *71*, 075109.

[48] I. Hamberg, C. G. Granqvist, *J. Appl. Phys.* **1986**, *60*, R123.

[49] D. Splith, S. Müller, H. von Wenckstern, M. Grundmann, *Proc. SPIE* **2018**, *10533*, 1.

[50] H. von Wenckstern, D. Splith, S. Lanzinger, F. Schmidt, S. Müller, P. Schlupp, R. Karsthof, M. Grundmann, *Adv. Electron. Mater.* **2015**, *1*, 1400026.